Local Plasmon Engineering in Doped Graphene

Fredrik S. Hage,[*,†] Trevor P. Hardcastle,[†,‡] Morten N. Gjerding,[§] Demie M. Kepaptsoglou,[†,△] Che R. Seabourne,[‡] Kirsten T. Winther,[§] Recep Zan,[⊥] Julian Alexander Amani,[¶] Hans C. Hofsaess,[¶] Ursel Bangert[‖], Kristian S. Thygesen[§] and Quentin M. Ramasse[*,†,‡,▲]

[†]SuperSTEM Laboratory, SciTech Daresbury Campus, Daresbury, WA4 4AD, U.K.
[‡]School of Chemical and Process Engineering, University of Leeds, Leeds, LS2 9JT, U.K.
[§]CAMD and Center for Nanostructured Graphene (CNG), Denmark Technical University, Fysikvej 1, building 307, 2800 Kgs. Lyngby, Denmark.
[△] York NanoCentre, University of York, Heslington, York, YO10 5BR, U.K.
[⊥]Nanotechnology Application and Research Center, Niğde Omer Halisdemir University, Niğde 51000, Turkey.
[¶]II Physikalisches Institut, Georg-August-Universität Göttingen, Friedrich-Hund-Platz 1, 37077 Göttingen, Germany.
[‖] Bernal Institute and Department of Physics, University of Limerick, Limerick, Ireland
[▲]School of Physics, University of Leeds, Leeds, LS2 9JT, U.K.

Keywords: STEM, EELS, plasmon, boron, nitrogen, graphene, DFT.

ABSTRACT: Single atom B or N substitutional doping in single-layer suspended graphene, realised by low energy ion implantation, is shown to induce a dampening or enhancement of the characteristic interband π plasmon of graphene through a high-resolution electron energy loss spectroscopy study in the scanning transmission electron microscope. A relative 16% decrease or 20% increase in the π plasmon quality factor is attributed to the presence of a single substitutional B or N atom dopant respectively. This modification is in both cases shown to be relatively localised, with data suggesting the plasmonic response tailoring can no longer be detected within experimental uncertainties beyond a distance of approximately 1 nm from the dopant. *Ab initio* calculations confirm the trends observed experimentally. Our results directly confirm the possibility of tailoring the plasmonic properties of graphene in the ultraviolet waveband, at the atomic scale, a crucial step in the

quest for utilising graphene's properties towards the development of plasmonic and optoelectronic devices operating at ultraviolet frequencies.

Due to its fascinating properties, graphene is emerging as a highly promising plasmonic material for implementation in devices aimed at applications such as chemical and molecular sensing, ultrafast optical modulation, non-linear optics, photo detection, light sources and quantum optics.[1-6] In the terahertz (THz) to mid-infrared (mid-IR) spectral range graphene plasmons are associated with the collective excitation of free charge carriers and exhibit a higher degree of tunability and mode confinement, as well as longer propagation distances than noble metals.[1-5] The graphene "charge carrier plasmon" frequency scales as $(E_F/D)^{0.5}$, where E_F is the Fermi energy and D is the size of the graphene sheet.[1, 4] This means that the plasmon frequency can be tuned by either varying the Fermi level (e.g. through electrostatic gating[4, 5, 7, 8] or chemical doping[2, 4, 5]), modifying the size of the graphene sheet[4] (e.g. by making micro to nanoscale graphene ribbons[4, 5] or discs[3, 5, 9]) or a combination of both. Using one or both these "methods" to push the charge carrier plasmon frequency into the near-IR to visible spectrum is of significant current interest in the community.[1, 3, 4, 10] Existing graphene-based IR plasmonic devices already exhibit promising properties, such as gate tuneable switching and control of the plasmon wavelength as well as a 40-60 times reduction in plasmon wavelength (as compared to the incident IR illumination).[7, 8] While these plasmons can propagate a distance on the order of a few times their own wavelength,[7, 8] on par with measurements of plasmons in Au,[8, 11] this falls short of that expected for high purity graphene.[7, 8] This has been attributed to disorder.[12] Indeed, the graphene charge carrier plasmon mobility is expected to decrease to various degrees depending on type and concentration of dopants[12, 13] and other defects,[14]

as well as the specific edge structures of nanoscale ribbons and similar nanoscale geometries.[4] Possible strategies for realisation of graphene based plasmonics in the near-IR to visible spectrum, while taking into consideration the above effects (among others), are discussed in Ref. [4]

At higher spectral frequencies, in the ultraviolet (UV) range, graphene exhibits interband plasmons resonances attributed to the collective oscillation of π and σ valence electrons.[15-17] These interband plasmons show a remarkable degree of sensitivity to various nano- to atomic-scale structures and defects in graphene: interband plasmon localisation has been attributed to confinement induced by edge states of a ~1.3 nm graphene quantum disc[18] and single substitutional Si atoms have been associated with a highly localised enhancement of the interband plasmon response.[19] In periodically rippled graphene (on a Ru(0001) surface) the interband π plasmon is confined to ripple "hills" while being significantly dampened in ripple "valleys".[20] Admittedly showing a more limited tunability compared to the charge carrier plasmon,[4] the interband π plasmon frequency is nonetheless predicted to progressively red-shift with increasing graphene nanodisc diameter, being the most sensitive to disc diameters below 20 nm.[21] However, with the exception of the above studies, reports on other aspects of the interband plasmon response of graphene are lacking in the literature. Such knowledge might open up avenues for future implementation of graphene based plasmonic and optoelectronic devices operating in the UV waveband. With this goal in mind, the present work investigates the modification of the interband plasmon response of graphene associated with two key substitutional dopants, namely boron and nitrogen atoms.

The inclusion of B or N atoms in the graphene lattice is the focus of extensive study in the scientific community, with the aim to modify the electronic structure of graphene.[22-29] Substitutional B and N atoms have been predicted to induce a shift of the Fermi level,[26, 29, 30] resulting in *p* or *n* doping akin to that routinely exploited in current semi-conductor technology. Indeed a *p* and *n* character has recently been verified in suspended graphene containing single substitutional B and N atom dopants.[29] Under certain circumstances, boron and nitrogen doping is also expected to induce a band gap in graphene.[24, 25].

Key to these proof-of-principle studies, electron energy loss spectroscopy (EELS) in combination with high angle annular dark field (HAADF) imaging in the aberration corrected scanning transmission electron microscope (STEM) are considered particularly useful techniques for identifying individual nano to atomic scale defects in a material and the associated effects on its electronic structure and dielectric response.[31] Due to the ideal 'gentle STEM'[32] combination of ultra-high vacuum conditions and low acceleration voltage (which minimises any beam-induced damage to the samples), individual B[23, 29] and N[23, 29, 33, 34] atom dopants in graphene can be identified directly in an ADF image. So-called "core" EEL spectra (EEL >≈ 50 eV) contain information about the local electronic structure and bonding in graphene,[28, 29, 33-35] while "valence" EEL spectra (EEL <≈ 50 eV) contain information about the graphene dielectric response[18, 19, 36-41]. In combination with simultaneous (STEM) ADF imaging, EEL spectra allow for a direct correlation of defect-induced modifications of the graphene electronic structure[28, 29, 33-35] and dielectric response[18, 19] with atomic scale structure. These capabilities mean STEM-EELS is an excellent technique for investigating the interband plasmon response induced by individual B and N atom dopants in graphene, as

this information can be correlated directly with the atomic structure, all within the same experiment.

In the valence loss spectrum of graphene the so-called "π peak" (~ 5 eV) is attributed primarily to the excitation of the π interband plasmon,[37, 39-43] superimposed on a sum over π-π* interband transitions.[37, 39-42] A recent controversy concerning the interpretation of the π peak[41, 44] was addressed in subsequent theoretical studies which show that (for STEM-EELS) the π loss peak is most appropriately interpreted as predominantly due to the excitation of the interband π plasmon of both doped[17] and dopant free[15, 16] graphene. In following with this, we use STEM-EELS to show that a single B or N substitutional atom dopant induces dampening or enhancement of the graphene interband π plasmon, respectively, with an estimated relative 16% decrease (B) or 20% increase (N) in quality factor, and, a ~1 nm localisation in both cases. This effect was observed independently using two separate STEM-EELS systems (with different yet complementary experimental parameters) and is significantly more pronounced than that previously reported for single Si atoms.[19]

Ab initio calculations were carried out on the largest supercells possible whilst keeping the computational costs tractable to validate the experimental results. While our theoretical spectra broadly reproduce the trends observed experimentally, it is suggested that the supercell sizes used in the present work (in practice limited by associated computational costs) are simply too small to accurately predict the relevant properties of the experimentally probed systems and faithfully reproduce all the details of the loss function.

Nevertheless, our combination of state-of-the-art experimental and theoretical results demonstrates that the plasmonic properties of graphene can be tailored at the atomic scale, using an implantation technique already extensively used in semi-conductor industry.[23, 29] Atomic scale plasmon engineering of graphene might prove valuable in the quest for utilising graphene's properties towards the development of plasmonic and optoelectronic devices operating in the UV waveband. Indeed, recent reports propose utilising the π interband plasmon response associated with graphene nanopores as a sensing mechanism for DNA nucleotides.[45, 46]

RESULTS

Dopant Induced Response

Figure 1 shows medium angle annular dark field (MAADF: see Methods section for the corresponding optical parameters) images of patches of B doped (Figure 1a) and N doped (Figure 1b) graphene acquired simultaneously with the corresponding valence loss spectra shown in Figures 1c and d. Following Refs.,[23, 29] the lower (higher) relative image intensity in the honeycomb lattice is attributed to the presence of an individual B (N) atom, indicated by the red (blue) arrow in Figure 1a (b). Figure S1 in the Supporting Information shows B-*K* and N-*K* ionisation edge maps of the same B and N atoms shown in Figure 1. B (N) doped valence loss spectra were acquired simultaneously with the images in Figure 1a (b). Each pixel in Figures 1a, b corresponds to one individual spectrum. Spectra from the B (N) doped patches shown in Figures 1c, d were integrated over the regions indicated by the red (blue) squares in Figure 1a (b).

Figure 2a shows a MAADF image of a single layer patch of non-doped graphene, where the top and bottom higher contrast regions correspond to carbonaceous material superimposed on the graphene sheet. Spectra in Figures 2b, c were integrated over regions 1-4 indicated in Figure 2a. Spectra from regions 1 and 3 are compared to those of the B and N doped samples in Figures 1c and d. Table 1 shows π peak energies and FWHMs extracted from the spectra in Figure 1c (see Methods).

The spectra in Figures 1c, d and Figures 2b, c contain a wealth of information which allows for an in-depth analysis of the effect of B and N doping on the graphene dielectric response. Perhaps the most striking result is shown in Figure 1c, where the background-subtracted normalised π peak of the valence loss spectrum exhibits an apparent significant modification of the dielectric response as a function of heteroatom doping. When compared to the non-doped sample, the spectra appear to indicate that the inclusion of a single B atom results in significant broadening of the π peak. Conversely, the inclusion of a single N atom appears to results in the π peak becoming significantly narrower.

Before continuing onto a detailed analysis of the spectra in Figure 1c, it is important to take into consideration any contributions to the spectra that can be attributed to factors other than the individual dopant atoms. Due to so-called *inelastic delocalisation*,[31] an incident electron has a finite probability of undergoing inelastic scattering some distance away from where the highly focused electron beam impacts the sample. The extent of inelastic delocalisation can be quantified in terms of the so-called localization diameter $d_{50} \approx 0.8\lambda \left(E_0 / E \right)^{3/4}$, [47] where E_0 is the incident electron energy, E is the energy loss and λ is the incident electron wavelength. The localization diameter gives the size of the area within

which 50% of inelastic scattering is expected to occur. For the π peak $d_{50}\left(\approx 5\ \mathrm{eV}\right) \approx 5\ \mathrm{nm}$, thus for accurate interpretation of the spectra in Figure 1c one needs to consider the sample composition several nm away from the electron beam position.

The bright contrast at the top and bottom of the MAADF image in Figure 2a shows the presence of carbonaceous disordered material covering an un-doped graphene patch. The same kind of carbonaceous disordered material surrounds all graphene patches (doped or otherwise) investigated in the present work (see also Figure S4 in the Supporting Information). Thus, it is crucial to determine any possible contribution of this carbonaceous material to the recorded valence loss spectra. This was done by serially acquiring individual spectra over the entire region shown in Figure 2a. These spectra were integrated over four selected regions (labelled "1"-"4", Figure 2a) with varying proximity to the carbonaceous material. Background-subtracted spectra from all four regions are normalised to the ~15 eV π+σ peak[15, 16, 37, 48] in Figure 2b. With decreasing distance to the carbonaceous material, the spectra in Figure 2b exhibit an increased intensity in the high energy shoulder of the π+σ peak. This is attributed to the contribution of the 22-23 eV π+σ peak of disordered carbon.[49] Figure 2c shows the effect of electron beam proximity to the carbonaceous material on the normalised π peak from regions 1 and 4. The appearance of a high energy loss ~6 eV shoulder in the spectrum from region "4" (indicated by the black arrow in Figure 2c) can clearly be attributed to the ~6.5 eV peak of disordered carbon.[49] Having established the likely spectral contributions of material surrounding the clean patches, the effect of doping in Figures 1c, d can now be evaluated.

Spectra normalised to the π+σ peak height are compared for non-doped (regions 1 and 3) and doped graphene in Figure 1d. Clearly there is a minor contribution of beam proximity to carbonaceous material in the B and N doped spectra in Figure 1d. This contribution matches exactly that of the non-doped graphene spectrum integrated over region 3 in Figure 2a. There are, however, significant differences between the π peaks of the B/N implanted samples and that of the non-doped sample. For N doped graphene, the π peak is significantly narrower than that of both non-doped spectra in Figure 1c. For B doped graphene, the π peak is significantly broader than that of both the non-doped spectra in Figure 1c. Moreover, there is broadening on both the high and low energy shoulders of the π peak for B doped graphene (Figure 1c), rather than only for the high energy shoulder as was observed for the non-doped spectra for regions 3 (Figure 1c) and 4 (Figure 2c). Thus the observed π peak width modification in the N and B doped spectra in Figure 1c is unambiguously different from the effects induced by the electron beam proximity to possible surrounding carbonaceous material discussed above, and provides a clear spectral fingerprint of the tailored plasmonic response of doped graphene.

In order to evaluate possible instrumental factors affecting the spectra (in Figure 1c), B and N doped, and, non-doped graphene loss spectra were also recorded using a lower energy resolution microscope (a non-monochromated Nion UltraSTEM100 microscope, see Figure S3c in the Supporting Information and Methods section) than the instrument on which the data presented on figures 1 and 2 were acquired (a monochromated Nion UltraSTEM100MC 'Hermes', which is capable of <15 meV energy resolution: see Methods section). The UltraSTEM100MC and UltraSTEM100 π peak spectra show excellent qualitative agreement (see the Supporting Information). These additional, independent observations

unambiguously validate the observed π peak modification for B(N) doped graphene (in Figure 1c) as experimentally meaningful and unrelated to instrumental factors.

In light of the above analysis, where proximity to surrounding carbonaceous material and instrumental factors are taken into careful consideration, we therefore conclude that the increase (decrease) in π loss peak width in Figure 1c can be unambiguously attributed to the incorporation of a single substitutional B (N) atom dopant in the graphene lattice, and a fingerprint of the tailoring of the doped graphene sheet's plasmonic response.

Localisation

An interesting aspect of dopant induced modification of the valence loss response of graphene is the degree to which such an effect is localised. Zhou *et al.*[19] reported a significant and highly localised increase in π and π+σ loss peak intensities upon incorporation of a single Si atom in a suspended graphene monolayer. This result was later confirmed by means of a combination of STEM-EELS and theoretical modelling.[50] As the present dopant-induced π peak modifications (shown in Figures 1c and S3c) are significantly more pronounced than the enhancement reported for a single Si atom,[19] one might expect a comparable degree of localisation to that reported by Zhou *et al.*[19] A combination of obfuscation by local variations in the overlapping ZLP tail intensity (due to fluctuations in the electron probe current) and spectrometer camera noise made it difficult to extract unambiguous localised information from the experimental data used to generate Figures 1 and S3. However, when optimising the experimental conditions to increase the signal-to-noise (at the cost of reducing the energy resolution to 450-500 meV, see Methods) the local variation in the valence loss response can be mapped at the nano-scale. Figure 3 shows

MAADF images and EELS maps of patches including a single N or B dopant. The EELS maps were integrated over energy regions dominated by the π peak (4.0-5.5 eV), the π+σ peak (13-25 eV), and the extended tail of the π+σ peak (26-43 eV and 44-60 eV). Both the 4.0-5.5 eV maps in Figure 3 are again dominated by the ZLP tail intensity due to fluctuations in the electron probe current and spectrometer camera noise, thus obfuscating any localised information. In contrast to the case of a single Si dopant,[19] no significant localised enhancement was observed for the π+σ peak of B and N doped graphene. However, the extended π+σ tail maps show an apparent atomically resolved contrast corresponding mostly to the graphene lattice (26-43 eV) and the dopant atoms (44-60 eV), in good general agreement with recent reports by Kapetanakis *et al.* on non-doped[51] and Si doped graphene.[50] The densities of states calculated for these two systems by Kepaptsoglou *et al.*[8] indeed predict a deficiency (resp. excess) density localised on the B (resp. N) dopant below the Fermi level, with further localised (or "resonant", to reprise Kapetenakis *et al.*'s terminology[50]) states unoccupied at high energy in the π* band, which would lead to the contrast observed experimentally.

In order to extract localised information about the B and N dopant-induced effects on the π peak, the datasets shown in Figure 3 were de-noised and the π peaks were fitted with a Gaussian (see Methods). Figures 4 a and d show extracted line profiles of the π peak FWHM compared to corresponding MAADF image intensities for N and B doped graphene, respectively, in the vertical direction (profiles labelled I and III, as indicated) and horizontal direction (profiles labelled II and IV, as indicated). The MAADF images and FWHM maps from which these line profiles were extracted are shown in Figures 4b, c (N) and e, f (B). Overview MAADF images in Figures 4g and h are presented as "duplicate pairs", where the

contrast is enhanced in the leftmost image of each pair in order to increase the visibility of the dopant atoms and the graphene lattice. The white rectangles in Figures 4 g, h indicate the confines of the regions from which the data in Figures 4a-c, d-f were acquired. The white arrows indicate the presence of disordered carbonaceous material superimposed on the graphene sheets, away from the dopants. The FWHM line profiles in Figure 4 show either a local minimum (Figure 4a) or maximum (Figure 4d) superimposed on a slowly increasing (Figure 4a) or decaying (Figure 4d) slope. Due to the limited energy resolution in these datasets where experimental parameters were adjusted to optimise signal-to-noise for 2D mapping, an unambiguous distinction between symmetric (*i.e.* dopant induced) and asymmetric (*i.e.* induced by proximity to carbonaceous material) broadening of the π peak was not feasible, in contrast to the datasets shown in Figures 1, 2 where, as discussed above, these effects can be unambiguously distinguished spectrally. Nevertheless, the local decrease (increase) in π peak FWHM, centred on the position of the respective individual N (B) atom dopant, clearly reproduces qualitatively the decrease (increase) in π peak FWHM in Figures 1c and S3c and is attributed to the incorporation of a single dopant. The spatial extent of the dopant-induced π peak modification can be estimated to ~1 nm in both cases from the line profiles in Figures 4a and d (with a larger error in linetraces II and IV due to the reduced size of the maps in these directions), and is also indicated on maps in Figures 4c and f with a dotted white circle as a guide to the eye. The much more slowly varying slopes of the FWHM line profiles are expected to arise from the contribution of the surrounding carbonaceous material, rather than the individual dopants. Indeed, these correlate visually with the presence of some carbonaceous material surrounding the single layer graphene patches in Figures 4g and h. Note that as de-noising through Principal Component Analysis

(PCA, see Methods section) was necessary for producing the maps in Figures 4 c, f, possible contributions of unintended artefacts induced by this process cannot be excluded altogether despite the care taken in order to minimise such effects. Moreover, as ΔE > 200 meV, the absolute π peak FWHM values in Figures 4 a, c, d, f are significantly affected by instrumental broadening (see the Supporting Information). Thus, the present ~1 nm localisation estimate would likely benefit from confirmation using a spectrometer camera with significantly better noise characteristics than those used in the present work. Such an experiment could make it possible to carry out spatially resolved measurements for which instrumental broadening would be negligible, thus also providing absolute π peak FWHM values.

First-Principles Modelling

For reliable prediction of the graphene loss spectrum it has been shown that at finite momentum transfer within density functional theory (DFT)[52, 53] it is necessary to invoke corrections for local field effects (LFEs) to the random phase approximation (RPA) loss function.[42] The inclusion of LFEs is justified by mixing of π-π* transitions (including those of the Dirac cone), explaining[42] why the observed[39-41] graphene π peak dispersion deviates significantly from that of graphite. Moreover, excitonic effects have been predicted to introduce significant corrections to the graphene optical absorption spectrum,[54-56] shifting for instance a major absorption peak from 5.1 eV to 4.5 eV.[54] Thus for a comprehensive understanding of the above experimental results a theoretical treatment beyond classical dielectric theory is imperative. It is important to emphasise, however, that building theoretical models of low-loss excitations which are representative of the excitations being probed in the microscope is a delicate and difficult matter. For example, the 50%

localisation diameter of the excitation at about 5 eV is about seven times larger than the lattice vector of the 3x3 supercells used in our calculations.

Another consequence of the relatively small supercells is that the lowest dopant concentration attainable, without any artificial adjustment of the doping level, is 1/18 = 5.6%, ~ 6 times higher than that of the samples studied in the microscope (estimated in Ref.[23]). A high carrier concentration leads to the emergence of an intraband plasmon which obscures the losses (and thus the lifetime) of the interband π-plasmon at large frequencies thus highlighting the importance of eliminating the intraband response. With these considerations in mind, theoretical calculations have been performed on supercells of sizes 3x3 containing a single B/N dopant including states up to +15 eV above the Fermi energy. The doping level was subsequently adjusted to the Dirac point such as to eliminate excess carriers induced by the B/N dopant and thus remove the intraband dielectric response. Calculations on 4x4 supercells were attempted but failed due to excessive memory requirements. Monkhorst-Pack *k* points grids of 36x36x1 were employed and the EEL spectrum was calculated by assuming an isotropic dielectric response so that 2D momentum integration can be reduced to a 1D integral. The validity of this assumption was tested by comparison to the full momentum integration, with a coarser sampling.

The results are shown in Figure 5. Full lines indicate local EEL spectra averaged over the entire 3x3 supercell. Dashed lines mark the q = 0 component of the EEL spectrum (where q = $|\vec{q}|$) which by comparison to the full lines give an idea of the importance of non-local effects. Red and blue lines indicate respectively B and N doping and the grey shaded area shows the reference pristine graphene spectrum. Generally the effect of including the non-local response is a blue-shift of the EEL spectral features. We point out that the pure graphene

spectra show a strong agreement with the momentum-resolved energy loss spectra found for freely-suspended single-layer pure graphene by Wachsmuth *et al.*,[40] exhibiting the same dispersion characteristics in the energy range considered. The theoretical pure graphene spectra presented in Figure 5 also show a strong resemblance to previously published theoretical studies[40, 57-59] with a shoulder in the range 1 – 3 eV consistent with single-particle $\pi \rightarrow \pi^*$ excitations and a strong excitation at about 5 eV.

For the doped cases, the comparison to experimental data is less straightforward. Relatively sharp features are observed at energies between 3-3.5 eV on the low energy side of the π peak in the simulated loss spectra, whereas such features were never observed experimentally, regardless of the energy resolution used for the acquisition. The sharp nature of these features, and the fact that they are not affected by the inclusion of higher momentum transfers in the calculation, suggest these can likely be attributed to single $\pi \rightarrow \pi^*$ transitions involving states created as an artefact due to the finite supercell size. Nonetheless, when comparing Figure 5 to our preliminary calculations in Figure S5 in the Supporting Information, it is clear that adjusting the doping level to the Dirac point goes a long way towards minimising artefacts induced by finite supercell size. By contrast, the high energy shoulder of the π peak at about 5 eV follows the experimental trend: when including a full summation over $\vec{q}$, the calculated B doped (resp. N doped) loss function is marginally broader (resp. narrower) than the undoped case. Interestingly, the calculations carried out in the optical limit show a less pronounced trend. This will be discussed in more detail below.

Considering the excellent match of our calculations of pure graphene with published theoretical *and* experimental studies, and the reproducibility of the experimental spectra

acquired on two different instruments in Figures 1c and S3c, it stands to reason that the moderate match to the experimental data in the doped cases in Figure 5 is due to the fact that calculations using 3×3 super cells are not a fully realistic representation of the single-dopant systems studied in the microscope(s). Increasing the super cell size to 4x4 is however not an option in practice since the memory demands increase drastically and would probably still not be sufficient for a direct comparison with the experimental STEM-EELS spectrum due to the relatively large localisation diameter. Thus the presented calculations were as thorough and using as high a level of detail as is currently possibly while keeping the computational costs tractable. In conclusion, given that the observed trends on the high energy side of the π peak reproduce those observed experimentally, we surmise that a calculation using a much larger supercell with a single dopant atom would likely improve this agreement and provide a more valid experiment/theory comparison. We surmise further that it is unlikely that a GW[60] or BSE[61] calculation on the supercells used in this study (currently computationally impractical) would yield a significantly different result; it has been shown that the standard ground state LDA electronic structure has strong overall similarity to that found using GW[59], albeit with small but important differences at the Dirac point. Thus, from a methodological point of view, in spite of merely reproducing trends rather than providing a 1:1 match with experimental results (arguably the ultimate goal of such calculations), the vast amount of numerical work summarised in Figure 5 could be thought of as a useful benchmark for further developments. Here, we include local field effects, compensate for altered carried concentration, and, importantly, include the convergent probe geometry in the final calculated spectra which has been shown to lead to exciting insights when comparing to experimental data.[62]

DISCUSSION

As discussed briefly above, the interpretation of the graphene valence loss π peak has recently been the matter of some controversy in the scientific community: while Liou *et al.*[41] reported a significant "2D plasmon character" for the π peak, Nelson *et al.*[44] attributed the π peak solely to the excitation of a single-particle interband transition.[44] The conflict between the apparently differing reports was resolved by Novko *et al.*[15] and Nazarov[16] for non-doped graphene by means of comprehensive theoretical modelling: for STEM-EELS the π peak can be attributed primarily to the excitation of the interband π plasmon of graphene. Kupčić *et al.*[17] showed that this also is the case for doped graphene.

In general, the degree to which the π peak can be attributed to a collective excitation is dependent on the magnitude of momentum transfer allowed to contribute to the spectrum.[15-17] According to Novko *et al.*[15], this can be understood as follows (for the sake of simplicity only the π peak is first considered): for very small wave vectors ($\vec{q}$) approaching the long wavelength limit ($\vec{q}\rightarrow 0$), the effect of dynamic screening is negligible, which means that the π peak can be attributed to π→π* interband transitions around the M point of the Brillouin zone. The π peak therefore follows a $\vec{q}^2$ dispersion given by band structure topology. With increasing $\vec{q}$ the efficiency of dynamic screening increases, which means that the π peak shifts to higher energies than those characteristic of a peak purely due to single particle π→π* excitations. For finite, intermediate, $\vec{q}$ values the π peak follows a $\sqrt{\vec{q}}$ dispersion characteristic of a 2D electron gas plasmon, and thus can be understood as being due to the excitation of a 2D collective mode. When LFEs were included in the calculations by Novko *et al.*[15], the real part of the dielectric function for the π peak approached, but did

not cross, zero. This and a predicted broad π peak shape in the "finite $\vec{q}$ regime" are both attributed to strong Landau dampening of the collective response. With increasing $\vec{q}$, the π peak dispersion slowly approaches that of an unscreened π→π* transition, while retaining the broad peak shape of the Landau damped plasmon region. Thus for large $\vec{q}$ values, the π peak again exhibits a significant single particle π→π* character.[15] This model is in good general agreement with the work of Nazarov.[16] For the π+σ peak the same basic description applies as that for the π peak above, albeit with the caveat that the π+σ peak comprises contributions from two separate σ→σ* transitions/ plasmons, thus somewhat complicating the situation.[15] Regardless, as all loss spectra in the present work were acquired by accepting spectral contributions over a large $\vec{q}$-range (*i.e.* from the long wavelength limit to beyond the first Brillouin zone), the present π and π+σ loss spectrum peaks are most appropriately interpreted as predominantly due to the excitation of Landau dampened interband plasmons in graphene.

Thus the observed modification of π peak width above (see Figures 1c, S3c and Tables 1, S1) can confidently be attributed to a significant dopant-induced modification of the interband π plasmon excitation lifetime.[31] Or in other words: the observed effects can be understood in terms of dampening or enhancement of the interband π plasmon of graphene. Despite having a predominantly collective character, the results presented above (see Figure 4) clearly show that the B (N) dopant induced π plasmon dampening (enhancement) is remarkably localised; the measured response is confined to a ~1 nm region centred on the single B (N) dopant atom. This degree of localisation is consistent with that reported for single Si atoms.[19]

Concerning the π+σ (EEL: 12- 25 eV) peak maps in Figure 3, the lack of a localised enhancement indicates that the associated interband σ plasmon(s) are largely unaffected by B or N doping, in stark contrast to the case of a substitutional Si atom.[19, 50] As discussed above, the highly localised response associated with energy losses comprising the extended tail of π+σ peak (in Figure 3) are attributed to single particle interband transitions, rather than the collective response. Thus, from the present results and above discussion it is concluded that in terms of collective valence electron response, single substitutional B and N dopants primarily affect the π valence electrons of suspended single layer graphene. Along the same lines, the presence of another type of substitutional defect (non-hexagonal rings) was recently shown to predominantly affect the interband π plasmon of single wall carbon nanotubes.[63]

A useful parameter for a more quantitative interpretation of plasmon dampening and enhancement is the dimensionless quality factor $Q \approx E_P/FWHM$, where E_P is the plasmon energy.[64] The lower the value of the Q factor, the higher the degree of collective mode dampening within a system. In order to minimize any error in the estimation of Q introduced by variations in spectral contribution from the carbonaceous material surrounding all investigated graphene patches, (using Table 1) B and N doped π plasmon quality factors were compared to that of the non-doped spectrum integrated over region 3 (see Figures 1, 2). While all three systems exhibit a π plasmon quality factor of ~ 3, absolute Q values are problematic to determine directly due to the contributions of superimposed π→π* interband transitions, among other factors. However, relative changes in Q can be estimated assuming the contribution of π→π* interband transitions remain largely unchanged upon B and N doping. Calculated band structures shown in Ref.[29] predict only

very minor modifications of the graphene π and π* band structure topology upon B and N doping. By extension, it is therefore suggested that the corresponding loss spectrum π→π* contribution will remain largely unaffected by B and N doping. From the values in Table 1, it is estimated that a single B dopant induces a 16% relative decrease in Q while a single N dopant induces a relative 20% increase in Q. As shown in, at an energy resolution of 200 meV or better the π peak width appears to be determined by excitation lifetime rather than instrumental broadening. Thus the contribution of instrumental broadening to the measured π plasmon quality factors is expected to be negligible in the present case.

From an intuitive, if simplistic, picture of the dopant-induced valence electron structure rearrangement, the observed effect for the π plasmon could be attributed to a reduction (increase) in the net π valence electron density induced by the incorporation of a single B (N) atom in the graphene lattice, within the framework of classical dielectric theory.[11, 17] However, as induced microscopic components of the dielectric response contribute significantly to the EEL π peak of graphene,[42] such an interpretation could be highly problematic. The microscopic response was taken into account by including LFEs in our *ab initio* calculations presented above (see Figure 5). While the theoretical spectra in Figure 5 broadly reproduce the experimental trends for the π plasmon peaks for the doped cases in Figures 1c and S3c, there are also significant discrepancies. Thus, a detailed analysis of the exact mechanism resulting in experimentally observed π plasmon dampening and enhancement is problematic, based on the present results alone.

In Figure 5, our calculations carried out in the optical limit show a less pronounced trend as compared to our calculations including a full summation over $\vec{q}$. This might, at least in part, provide an explanation for the discrepancy between the EELS results shown here and the

optical conductivity results of Mak *et al.*[56], who, in a combined experimental and theoretical study, showed simultaneous broadening and red-shift of the π peak upon both *p* and *n* doping. Similarly, a red-shift for the optical absorption spectrum π peak of graphene upon *n* doping has been predicted by Yang *et al*.[55] Conventional optical absorption measurements probe the single particle π→π*character of the π peak (se *e.g.* Ref. [48]), while STEM-EELS probes predominantly the collective (finite $\vec{q}$) response of the π valence electrons.[15-17] Thus the discrepancies between the present data and that of Ref. [56] could be rationalised by the present results reflecting primarily the induced collective response, rather than solely the response associated with dopant induced single particle transitions. As doping of graphene in a field effect transistor setup (Mak *et al.*[56]) and by B/N implantation[26, 29] (present work) both primarily result in Fermi level shifts, differences in sample composition are expected to contribute to a lesser degree.

Controllable doping of our graphene samples was achieved by means of low energy ion implantation.[23, 29] Compared to earlier demonstrations of N or B doping *via* chemical routes,[65] ion implantation of graphene shows great promise for modifying its electronic properties at the industrial scale due to the possibility of incorporating this processing step directly in existing flexible small-depth channel doping apparatus, already used extensively in the semi-conductor industry.[23, 29] Thus our results not only demonstrate that single atom B or N dopants in graphene induce a highly localised dampening or enhancement of the interband π plasmon, but also that these modifications of the dielectric response can be achieved using a process compatible with current industry. By extension, carefully controlling the position and number of single B or N atoms, or both, could open the door to atomic scale plasmonic engineering: forming conduits and more complex functional

geometries in graphene-based devices for plasmonic and optoelectronic applications operating at UV frequencies. As a relevant example, the local response of the interband π plasmons associated with graphene nanopores has been proposed as the basis for a device for sensing mechanism for DNA nucleotides.[38, 39]

CONCLUSION

Using two separate dedicated STEM-EELS systems, it is demonstrated that a single atom B or N substitutional dopant respectively induces a quantifiable dampening or enhancement of the interband π plasmon of suspended graphene. A 16% decrease in π plasmon quality factor was measured for a single B atom dopant, while a 20% increase in π plasmon quality factor was measured for a single N atom dopant. The localisation of the dopant induced effect is estimated to ~1 nm, in both cases. For analysis of the loss spectrum π plasmon peak of graphene, instrumental broadening was deemed negligible for an energy resolution of 200 meV or better. Although trends are broadly reproduced by theory, the relative mismatch between experimental spectra and modelled *ab initio* spectra of the doped systems is attributed to practical computational limitations; larger supercell sizes (currently computationally impractical) are needed in simulations for an accurate comparison with experiments. Nonetheless, the present experimental data clearly demonstrate atomic scale modification of the plasmonic response of graphene, using an implantation technique compatible with current semi-conductor industry. Such atomic scale plasmonic engineering might prove valuable for developing graphene based plasmonic and optoelectronic devices operating in the UV waveband.

METHODS

Materials and Sample Preparation

Boron and nitrogen ion implantation was carried out using the Göttingen mass-selected ion beam deposition system (25 eV implantation energy). Graphene films placed on TEM grids were irradiated at room temperature in vacuum (2 x 10^{-6} Pa). Further details of the procedure are given by Bangert *et al.*[23] and references therein. A commercially available non-doped reference sample (Graphenea[66]) was investigated as a control experiment.

Scanning Transmission Electron Microscopy

All EEL spectra and images were acquired using one of two dedicated aberration corrected STEMs: either a Nion UltraSTEM100 equipped with a Gatan Enfina EEL spectrometer or a Nion UltraSTEM100MC equipped with a Gatan Enfinium ERS spectrometer optimised for high energy resolution using ultra-stable electronics. The microscopes are referred to as either "NUS100" or "NUS100MC" in the text. Both microscopes were operated at an acceleration voltage of 60 kV, which is below the knock-on damage threshold for graphene and is known to minimise any risk of electron-beam damage to the specimens, even after long, repeated exposure, and thus to provide ideal conditions for single atom spectroscopy.[32] For the NUS100 measurements, the electron probe convergence semi-angle (α) was 31 mrad and the spectrometer collection semi-angle (β) was 3 mrad, with an estimated probe size of 1.1 Å. For the NUS100MC α = 31 mrad, resulting in an estimated probe size of 1.0 Å, and β = 44 mrad (valence loss spectra) or β = 60 mrad (core loss spectra). The energy resolution (ΔE) in EELS is commonly given by the full-width at half-maximum (FWHM) of the quasi-elastic "Zero Loss Peak" (ZLP). For the NUS100 ΔE is given by

the native cold field emission source energy spread, and provided it is not limited by the spectrometer camera binning and point spread function, results in an effective resolution ΔE = 350 meV. While the source monochromator of the NUS100MC allows for reducing ΔE down to 13 meV while retaining atomic resolution (at an acceleration voltage of 60 kV)[67, 68] an energy resolution of 200 meV was found to be sufficient for making the contribution of instrumental broadening negligible for the NUS100MC π peak loss spectra (see Figure S2 in the Supporting Information). For the present work ΔE = 200 meV in Figures 1, 2, ΔE = 400 meV (N-*K* map) and ΔE = 200 meV (B-*K* map) in Figure S1, ΔE = 400 meV, 200 meV and 80 meV in Figure S2, and, ΔE = 450 meV (B doped) and ΔE = 500 meV (N doped) in Figures 3, 4.

All HAADF and medium angle annular dark field (MAADF) images presented are raw data, for which only contrast, brightness and field of view have been adjusted. Image detector semi-angles are: NUS100: 89-195 mrad (HAADF) and 54-85 mrad (MAADF), and, NUS100MC: 82-195 mrad (HAADF) and 59-82 mrad (MAADF). All ZLP subtraction was done using a power law fitted to the ZLP tail in the regions 1.80-2.05 eV for all the NUS100 valence loss spectra (Figure 3), 2.00-2.25 eV for the NUS100MC ΔE = 200 meV valence loss spectra (Figures 1, 3), 3.05-3.55 eV (B doped) and 3.6-4.1 eV (N doped) in Figure 4.

The spectra in Figures 1c, S3c were fitted using two Gaussians: one fitting the main π plasmon peak and one fitting the low energy tail attributed to π-π* interband transitions.[42] Results from respective peak fits are shown in Tables 1 and S1. The issue of ZLP extraction error was minimised by means of comprehensively testing a multitude of methods,[31, 69, 70] all providing similar results. As reported for multilayer graphene cones,[70] subtracting the ZLP tail by a fitted power law background was in the present case deemed optimal, yielding the

best compromise between accuracy of subtraction and spectral noise. The uncertainties of the fitted peak values in Tables 1, S1 are primarily attributed to choice of fitting function and parameters. Precisely determining the errors associated with choice of fitting parameters is problematic; however estimated non-standard errors determined by measuring peak values from the extremes of acceptable fits are given in Tables 1 and S1.

NUS100MC core loss spectra were de-noised using principal component analysis (PCA) as implemented in the MSA plug-in for Gatan's Digital Micrograph software suite.[71] For the valence loss EELS data, PCA de-nosing was only carried out on the loss spectrum images from which extracted data is shown in Figure 4. Great care was taken to minimise possible artefacts induced by the de-nosing process; the raw, reconstructed and residual spectral image datasets were compared in detail. For Figures 3, 4, EELS data was acquired using Gatan's "DualEELS" feature: two spectra were acquired in rapid succession for each beam position (represented by the individual pixels in the maps in Figures 3 and 4c, f): in one spectrum the signal-to-noise ratio was optimised by shifting the ZLP off the camera and by increasing the acquisition time so as to reach the camera saturation limit, while the accompanying spectrum included the full ZLP peak and was acquired at a much shorter exposure time so that the camera was far from saturation, thus minimising afterglow effects. The EELS maps in Figure 3 were produced by simple integration over the energy loss regions of the raw data indicated in Figure 3. In order to map the local variations in the π peak response in Figure 4, the ZLP tail was subtracted by fitting of a power-law function (after de-nosing) and the π peaks of the resulting spectra were fitted with a single Gaussian function throughout the datasets, using an automated procedure in Digital Micrograph. Fitting the π peaks with more than one Gaussian resulted in less reliable fits, which is

attributed to a relative increase in ZLP tail contribution as compared to the valence loss spectra in Figures 1, 2, S2 and S3.

First-Principles Calculations

The local density approximation (LDA)[53] exchange-correlation functional was used to optimise the graphene unit cell with a kinetic energy cut-off of 380 eV, a Monkhorst-Pack[72] *k*-points grid of 36×36×1 with in-plane spacings of 0.013 Å^{-1} and a 20 Å vacuum. The lattice parameter was found to converge to 2.44 Å and then used to construct the hexagonal supercells. The lattice vectors of all such supercells were then fixed, and the structures fully relaxed using BFGS[73-77] optimisation. The electron energy loss spectra of the relaxed structures were then found using the electronic structure code GPAW[78] which substitutes the Kohn-Sham wave functions, energy eigenvalues and occupations into the Adler-Wiser[27, 28] formula to calculate the Fourier coefficients of the non-interacting density response function, $\chi^0_{\vec{G}\vec{G}'}(\vec{q},\omega)$, where $\vec{G}$ is a given reciprocal lattice vector, $\vec{q}$ is the scattering wavevector, ω is frequency, and the zero in superscript signifies the non-interacting nature of the Kohn-Sham wavefunctions used to construct χ. Within the RPA, the dielectric matrix is then obtained by writing ε as:

$$\varepsilon^{RPA}_{\acute{G}\acute{G}'}(\acute{q},\omega) = \delta_{\acute{G}\acute{G}'} - \left(\frac{4\pi}{|\acute{q}+\acute{G}|^2}\right)\chi^0_{\acute{G}\acute{G}'}(\acute{q},\omega)$$

where $\frac{4\pi}{|\acute{q}+\acute{G}|^2}$ is the Coulomb potential, and $\chi^0_{\acute{G}\acute{G}'}$ is the non-interacting density response function. The dielectric matrix is then inverted to produce the EEL spectrum, including local field effects (LFEs). A local EEL spectrum can be obtained by calculating the response of a

material to a fast travelling electron as described by Nerl *et al.*[62] in their work probing the local nature of excitons and plasmons in few-layer MoS_2. Further details of the method have been described by Yan *et al.*[79]

ASSOCIATED CONTENT

Supporting Information

NUS100MC: STEM-EEL core loss maps of the B and N dopants shown in Figure 1 (Figure S1), valence loss spectra of non-doped graphene acquired at energy resolutions of 400-80 meV (Figure S2). NUS100: HAADF images and valence EEL spectra of B/N doped and non-doped graphene (Figures S3-4), and, estimated π peak energies and FWHMs (Table S1).

AUTHOR INFORMATION

Corresponding Authors

*Phone: +44 (0)1925 864 907. Fax: +44 (0) 1925 864 910. Email: qmramasse@superstem.org.

*Phone: +44 (0)1925 864 903. Fax: +44 (0) 1925 864 910. E-mail: fshage@superstem.org.

ACKNOWLEDGEMENTS

SuperSTEM is the UK Engineering and Physical Sciences Research Council (EPSRC) National Research Facility for Advanced Electron Microscopy. T.P. Hardcastle gratefully acknowledges the EPSRC Doctoral Prize Fellowship which funded this research in part. F.S. Hage and Q.M. Ramasse thank Dr J.C. Idrobo for useful discussions. The Center for Nanostructured Graphene is sponsored by the Danish National Research Foundation, Project DNRF103.

REFERENCES

(1) Xiao, S.; Zhu, X.; Li, B.-H.; Mortensen, N. A., Graphene-Plasmon Polaritons: From Fundamental Properties to Potential Applications. *Front. Phys.* **2016**, 11, 117801.

(2) Giovanni, V.; Tobias, W.; Jari, K.; Mikael, F., Graphene Plasmons in the Presence of Adatoms. *New J. Phys.* **2017**, 19, 073027.

(3) Huang, S.; Song, C.; Zhang, G.; Yan, H., Graphene Plasmonics: Physics and Potential Applications. *Nanophotonics* **2017**, 6, 1191-1204.

(4) García de Abajo, F. J., Graphene Plasmonics: Challenges and Opportunities. *ACS Photonics* **2014**, 1, 135-152.

(5) Grigorenko, A. N.; Polini, M.; Novoselov, K. S., Graphene Plasmonics. *Nat. Photonics* **2012**, 6, 749-758.

(6) Low, T.; Chaves, A.; Caldwell, J. D.; Kumar, A.; Fang, N. X.; Avouris, P.; Heinz, T. F.; Guinea, F.; Martin-Moreno, L.; Koppens, F., Polaritons in Layered Two-Dimensional Materials. *Nat. Mater.* **2017**, 16, 182-194.

(7) Chen, J.; Badioli, M.; Alonso-González, P.; Thongrattanasiri, S.; Huth, F.; Osmond, J.; Spasenović, M.; Centeno, A.; Pesquera, A.; Godignon, P.; Zurutuza Elorza, A.; Camara, N.; de Abajo, F. J. G.; Hillenbrand, R.; Koppens, F. H. L., Optical Nano-Imaging of Gate-Tunable Graphene Plasmons. *Nature* **2012**, 487, 77-81.

(8) Fei, Z.; Rodin, A. S.; Andreev, G. O.; Bao, W.; McLeod, A. S.; Wagner, M.; Zhang, L. M.; Zhao, Z.; Thiemens, M.; Dominguez, G.; Fogler, M. M.; Neto, A. H. C.; Lau, C. N.; Keilmann, F.; Basov, D. N., Gate-Tuning of Graphene Plasmons Revealed by Infrared Nano-Imaging. *Nature* **2012**, 487, 82-85.

(9) Koppens, F. H. L.; Chang, D. E.; García de Abajo, F. J., Graphene Plasmonics: A Platform for Strong Light–Matter Interactions. *Nano Lett.* **2011**, 11, 3370-3377.

(10) Cocchi, C.; Prezzi, D.; Ruini, A.; Benassi, E.; Caldas, M. J.; Corni, S.; Molinari, E., Optical Excitations and Field Enhancement in Short Graphene Nanoribbons. *J. Phys. Chem. Lett.* **2012**, 3, 924-929.

(11) Dallapiccola, R.; Dubois, C.; Gopinath, A.; Stellacci, F.; Negro, L. D., Near-Field Excitation and Near-Field Detection of Propagating Surface Plasmon Polaritons on Au Waveguide Structures. *Appl. Phys. Lett.* **2009**, 94, 243118.

(12) Principi, A.; Vignale, G.; Carrega, M.; Polini, M., Impact of Disorder on Dirac Plasmon Losses. *Phys. Rev. B* **2013**, 88, 121405.

(13) Novko, D., Dopant-Induced Plasmon Decay in Graphene. *Nano Lett.* **2017**, 17, 6991-6996.

(14) Luo, W.; Cai, W.; Wu, W.; Xiang, Y.; Ren, M.; Zhang, X.; Xu, J., Tailorable Reflection of Surface Plasmons in Defect Engineered Graphene. *2D Mater.* **2016**, 3, 045001.

(15) Novko, D.; Despoja, V.; Šunjić, M., Changing Character of Electronic Transitions in Graphene: From Single-Particle Excitations to Plasmons. *Phys. Rev. B* **2015**, 91, 195407.

(16) Nazarov, V. U., Electronic Excitations in Quasi-2D Crystals: What Theoretical Quantities Are Relevant to Experiment? *New J. Phys.* **2015**, 17, 073018.

(17) Kupčić, I.; Nikšić, G.; Rukelj, Z.; Pelc, D., Effective Numbers of Charge Carriers in Doped Graphene: Generalized Fermi Liquid Approach. *Phys. Rev. B* **2016**, 94, 075434.

(18) Zhou, W.; Pennycook, S., J.; Idrobo, J.-C., Probing the Electronic Structure and Optical Response of a Graphene Quantum Disk Supported on Monolayer Graphene. *J. Phys.: Condens. Matter* **2012**, 24, 314213.

(19) Zhou, W.; Lee, J.; Nanda, J.; Pantelides, S. T.; Pennycook, S. J.; Idrobo, J.-C., Atomically Localized Plasmon Enhancement in Monolayer Graphene. *Nat. Nanotechnol.* **2012**, 7, 161-165.

(20) Politano, A.; Campi, D.; Formoso, V.; Chiarello, G., Evidence of Confinement of the π Plasmon in Periodically Rippled Graphene on Ru(0001). *Phys. Chem. Chem. Phys.* **2013**, 15, 11356-11361.

(21) Hu, J.; Zeng, H.; Wang, C.; Li, Z.; Kan, C.; Liu, Y., Interband π Plasmon of Graphene: Strong Small-Size and Field-Enhancement Effects. *Phys. Chem. Chem. Phys.* **2014**, 16, 23483-23491.

(22) Zhang, C.; Fu, L.; Liu, N.; Liu, M.; Wang, Y.; Liu, Z., Synthesis of Nitrogen-Doped Graphene Using Embedded Carbon and Nitrogen Sources. *Adv. Mater.* **2011**, 23, 1020-1024.

(23) Bangert, U.; Pierce, W.; Kepaptsoglou, D. M.; Ramasse, Q.; Zan, R.; Gass, M. H.; Van den Berg, J. A.; Boothroyd, C. B.; Amani, J.; Hofsäss, H., Ion Implantation of Graphene—Toward IC Compatible Technologies. *Nano Lett.* **2013**, 13, 4902-4907.

(24) Casolo, S.; Martinazzo, R.; Tantardini, G. F., Band Engineering in Graphene with Superlattices of Substitutional Defects. *J. Phys. Chem. C* **2011**, 115, 3250-3256.

(25) Zhou, Y.-C.; Zhang, H.-L.; Deng, W.-Q., A 3 N Rule for the Electronic Properties of Doped Graphene. *Nanotechnology* **2013**, 24, 225705.

(26) Panchakarla, L. S.; Subrahmanyam, K. S.; Saha, S. K.; Govindaraj, A.; Krishnamurthy, H. R.; Waghmare, U. V.; Rao, C. N. R., Synthesis, Structure, and Properties of Boron- and Nitrogen-Doped Graphene. *Adv. Mater.* **2009**, 21, 4726-4730.

(27) Wang, H.; Maiyalagan, T.; Wang, X., Review on Recent Progress in Nitrogen-Doped Graphene: Synthesis, Characterization, and Its Potential Applications. *ACS Catal.* **2012**, 2, 781-794.

(28) Ramasse, Q. M.; Seabourne, C. R.; Kepaptsoglou, D.-M.; Zan, R.; Bangert, U.; Scott, A. J., Probing the Bonding and Electronic Structure of Single Atom Dopants in Graphene with Electron Energy Loss Spectroscopy. *Nano Lett.* **2013**, 13, 4989-4995.

(29) Kepaptsoglou, D.; Hardcastle, T. P.; Seabourne, C. R.; Bangert, U.; Zan, R.; Amani, J. A.; Hofsäss, H.; Nicholls, R. J.; Brydson, R. M. D.; Scott, A. J.; Ramasse, Q. M., Electronic Structure Modification of Ion Implanted Graphene: The Spectroscopic Signatures of p- and n-Type Doping. *ACS Nano* **2015**, 9, 11398-11407.

(30) Schiros, T.; Nordlund, D.; Pálová, L.; Prezzi, D.; Zhao, L.; Kim, K. S.; Wurstbauer, U.; Gutiérrez, C.; Delongchamp, D.; Jaye, C.; Fischer, D.; Ogasawara, H.; Pettersson, L. G. M.; Reichman, D. R.; Kim, P.; Hybertsen, M. S.; Pasupathy, A. N., Connecting Dopant Bond Type with Electronic Structure in N-Doped Graphene. *Nano Lett.* **2012**, 12, 4025-4031.

(31) Egerton, R. F., *Electron Energy-Loss Spectroscopy in the Electron Microscope*. Springer US: New York, 2011.

(32) Krivanek, O. L.; Zhou, W.; Chisholm, M. F.; Idrobo, J. C.; Lovejoy, T. C.; Ramasse, Q. M.; Dellby, N., Gentle STEM of Single Atoms: Low keV Imaging and Analysis at Ultimate Detection Limits. In *Low Voltage Electron Microscopy: Principles and Applications*, Bell, D. C.; Erdmann, N., Eds. John Wiley & Sons, Ltd: Chichester, UK, 2012; pp 119-161.

(33) Nicholls, R. J.; Murdock, A. T.; Tsang, J.; Britton, J.; Pennycook, T. J.; Koós, A.; Nellist, P. D.; Grobert, N.; Yates, J. R., Probing the Bonding in Nitrogen-Doped Graphene Using Electron Energy Loss Spectroscopy. *ACS Nano* **2013**, 7, 7145-7150.

(34) Lin, Y.-C.; Teng, P.-Y.; Yeh, C.-H.; Koshino, M.; Chiu, P.-W.; Suenaga, K., Structural and Chemical Dynamics of Pyridinic-Nitrogen Defects in Graphene. *Nano Lett.* **2015**, 15, 7408-7413.

(35) Suenaga, K.; Koshino, M., Atom-by-Atom Spectroscopy at Graphene Edge. *Nature* **2010**, 468, 1088-1090.

(36) Bangert, U.; Pierce, W.; Boothroyd, C.; Pan, C. T.; Gwilliam, R., Collective Electronic Excitations in the Ultra Violet Regime in 2-D and 1-D Carbon Nanostructures Achieved by the Addition of Foreign Atoms. *Sci. Rep.* **2016**, 6, 27090.

(37) Eberlein, T.; Bangert, U.; Nair, R. R.; Jones, R.; Gass, M.; Bleloch, A. L.; Novoselov, K. S.; Geim, A.; Briddon, P. R., Plasmon Spectroscopy of Free-Standing Graphene Films. *Phys. Rev. B* **2008**, 77, 233406.

(38) Gass, M. H.; Bangert, U.; Bleloch, A. L.; Wang, P.; Nair, R. R.; Geim, A. K., Free-Standing Graphene at Atomic Resolution. *Nat. Nanotechnol.* **2008**, 3, 676-681.

(39) Kinyanjui, M. K.; Kramberger, C.; Pichler, T.; Meyer, J. C.; Wachsmuth, P.; Benner, G.; Kaiser, U., Direct Probe of Linearly Dispersing 2D Interband Plasmons in a Free-Standing Graphene Monolayer. *Europhys. Lett.* **2012**, 97, 57005.

(40) Wachsmuth, P.; Hambach, R.; Kinyanjui, M. K.; Guzzo, M.; Benner, G.; Kaiser, U., High-Energy Collective Electronic Excitations in Free-Standing Single-Layer Graphene. *Phys. Rev. B* **2013**, 88, 075433.

(41) Liou, S. C.; Shie, C. S.; Chen, C. H.; Breitwieser, R.; Pai, W. W.; Guo, G. Y.; Chu, M. W., π Plasmon Dispersion in Free-Standing Graphene by Momentum-Resolved Electron Energy-Loss Spectroscopy. *Phys. Rev. B* **2015**, 91, 045418.

(42) Kramberger, C.; Hambach, R.; Giorgetti, C.; Rümmeli, M. H.; Knupfer, M.; Fink, J.; Büchner, B.; Reining, L.; Einarsson, E.; Maruyama, S.; Sottile, F.; Hannewald, K.; Olevano, V.; Marinopoulos, A. G.; Pichler, T., Linear Plasmon Dispersion in Single-Wall Carbon Nanotubes and the Collective Excitation Spectrum of Graphene. *Phys. Rev. Lett.* **2008**, 100, 196803.

(43) Wachsmuth, P.; Hambach, R.; Benner, G.; Kaiser, U., Plasmon Bands in Multilayer Graphene. *Phys. Rev. B* **2014**, 90, 235434.

(44) Nelson, F. J.; Idrobo, J.-C.; Fite, J. D.; Mišković, Z. L.; Pennycook, S. J.; Pantelides, S. T.; Lee, J. U.; Diebold, A. C., Electronic Excitations in Graphene in the 1–50 eV Range: The π and π + σ Peaks Are Not Plasmons. *Nano Letters* **2014**, 14, 3827-3831.

(45) Fotouhi, B.; Ahmadi, V.; Abasifard, M.; Roohi, R., Interband π Plasmon of Graphene Nanopores: A Potential Sensing Mechanism for DNA Nucleotides. *J. Phys. Chem. C* **2016**, 120, 13693-13700.

(46) Fotouhi, B.; Ahmadi, V.; Faramarzi, V., Nano-Plasmonic-Based Structures for DNA Sequencing. *Opt. Lett.* **2016**, 41, 4229-4232.

(47) Egerton, R. F., New Techniques in Electron Energy-Loss Spectroscopy and Energy-Filtered Imaging. *Micron* **2003**, 34, 127-139.

(48) Marinopoulos, A. G.; Reining, L.; Olevano, V.; Rubio, A.; Pichler, T.; Liu, X.; Knupfer, M.; Fink, J., Anisotropy and Interplane Interactions in the Dielectric Response of Graphite. *Phys. Rev. Lett.* **2002**, 89, 076402.

(49) Daniels, H.; Brydson, R.; Rand, B.; Brown, A., Investigating Carbonization and Graphitization Using Electron Energy Loss Spectroscopy (EELS) in the Transmission Electron Microscope (TEM). *Philos. Mag.* **2007**, 87, 4073-4092.

(50) Kapetanakis, M. D.; Oxley, M. P.; Zhou, W.; Pennycook, S. J.; Idrobo, J.-C.; Pantelides, S. T., Signatures of Distinct Impurity Configurations in Atomic-Resolution Valence Electron-Energy-Loss Spectroscopy: Application to Graphene. *Phys. Rev. B* **2016**, 94, 155449.

(51) Kapetanakis, M. D.; Zhou, W.; Oxley, M. P.; Lee, J.; Prange, M. P.; Pennycook, S. J.; Idrobo, J. C.; Pantelides, S. T., Low-Loss Electron Energy Loss Spectroscopy: An Atomic-Resolution Complement to Optical Spectroscopies and Application to Graphene. *Phys. Rev. B* **2015**, 92, 125147.

(52) Hohenberg, P.; Kohn, W., Inhomogeneous Electron Gas. *Phys. Rev.* **1964**, 136, B864-B871.

(53) Kohn, W.; Sham, L. J., Self-Consistent Equations Including Exchange and Correlation Effects. *Phys. Rev.* **1965**, 140, A1133-A1138.

(54) Yang, L.; Deslippe, J.; Park, C.-H.; Cohen, M. L.; Louie, S. G., Excitonic Effects on the Optical Response of Graphene and Bilayer Graphene. *Phys. Rev. Lett.* **2009**, 103, 186802.

(55) Yang, L., Excitonic Effects on Optical Absorption Spectra of Doped Graphene. *Nano Lett.* **2011**, 11, 3844-3847.

(56) Mak, K. F.; da Jornada, F. H.; He, K.; Deslippe, J.; Petrone, N.; Hone, J.; Shan, J.; Louie, S. G.; Heinz, T. F., Tuning Many-Body Interactions in Graphene: The Effects of Doping on Excitons and Carrier Lifetimes. *Phys. Rev. Lett.* **2014**, 112, 207401.

(57) Yan, J.; Thygesen, K. S.; Jacobsen, K. W., Nonlocal Screening of Plasmons in Graphene by Semiconducting and Metallic Substrates: First-Principles Calculations. *Phys. Rev. Lett.* **2011**, 106, 146803.

(58) Yuan, S.; Roldán, R.; Katsnelson, M. I., Excitation Spectrum and High-Energy Plasmons in Single-Layer and Multilayer Graphene. *Phys. Rev. B* **2011**, 84, 035439.

(59) Trevisanutto, P. E.; Giorgetti, C.; Reining, L.; Ladisa, M.; Olevano, V., *Ab Initio* GW Many-Body Effects in Graphene. *Phys. Rev. Lett.* **2008**, 101, 226405.

(60) Hedin, L., New Method for Calculating the One-Particle Green's Function with Application to the Electron-Gas Problem. *Phys. Rev.* **1965**, 139, A796-A823.

(61) Salpeter, E. E.; Bethe, H. A., A Relativistic Equation for Bound-State Problems. *Phys. Rev.* **1951**, 84, 1232-1242.

(62) Nerl, H. C.; Winther, K. T.; Hage, F. S.; Thygesen, K. S.; Houben, L.; Backes, C.; Coleman, J. N.; Ramasse, Q. M.; Nicolosi, V., Probing the Local Nature of Excitons and Plasmons in Few-Layer MoS2. *npj 2D Mater. Appl.* **2017**, 1, 2.

(63) Hage, F. S.; Hardcastle, T. P.; Scott, A. J.; Brydson, R.; Ramasse, Q. M., Momentum- and Space-Resolved High-Resolution Electron Energy Loss Spectroscopy of Individual Single-Wall Carbon Nanotubes. *Phys. Rev. B* **2017**, 95, 195411.

(64) Bosman, M.; Ye, E.; Tan, S. F.; Nijhuis, C. A.; Yang, J. K. W.; Marty, R.; Mlayah, A.; Arbouet, A.; Girard, C.; Han, M.-Y., Surface Plasmon Damping Quantified with an Electron Nanoprobe. *Sci. Rep.* **2013**, 3, 1312.

(65) Meyer, J. C.; Kurasch, S.; Park, H. J.; Skakalova, V.; Künzel, D.; Groß, A.; Chuvilin, A.; Algara-Siller, G.; Roth, S.; Iwasaki, T.; Starke, U.; Smet, J. H.; Kaiser, U., Experimental Analysis of Charge Redistribution due to Chemical Bonding by High-Resolution Transmission Electron Microscopy. *Nat. Mater.* **2011**, 10, 209-215.

(66) *URL: https://www.graphenea.com/*.

(67) Nicholls, R.; Hage, F. S.; Yates, J.; McCulloch, D.; Kepaptsoglou, D. M.; Lovejoy, T. C.; Dellby, N.; Krivanek, O. L.; Refson, K.; Ramasse, Q. M., Vibrational Phonon Spectroscopy of Boron Nitride Polymorphs: A Comparison Between Theory and Experiment. *Microsc. Microanal.* **2015**, 21, 1469-1470.

(68) Ramasse, Q. M., Twenty Years After: How “Aberration Correction in the STEM” Truly Placed a “A Synchrotron in a Microscope". *Ultramicroscopy* **2017**, 180, 41-51.

(69) Aguiar, J. A.; Reed, B. W.; Ramasse, Q. M.; Erni, R.; Browning, N. D., Quantifying the Low-Energy Limit and Spectral Resolution in Valence Electron Energy Loss Spectroscopy. *Ultramicroscopy* **2013**, 124, 130-138.

(70) Hage, F. S.; Ramasse, Q. M.; Kepaptsoglou, D. M.; Prytz, Ø.; Gunnaes, A. E.; Helgesen, G.; Brydson, R., Topologically Induced Confinement of Collective Modes in Multilayer Graphene Nanocones Measured by Momentum-Resolved STEM-VEELS. *Phys. Rev. B* **2013**, 88, 155408.

(71) Watanabe, M.; Kanno, M.; Ackland, D.; Kiely, C.; Williams, D., Applications of Electron Energy-Loss Spectrometry and Energy Filtering in an Aberration-Corrected JEM-2200FS STEM/TEM. *Microsc. Microanal.* **2007**, 13, 1264-1265.

(72) Monkhorst, H. J.; Pack, J. D., Special Points for Brillouin-Zone Integrations. *Phys. Rev. B* **1976**, 13, 5188-5192.

(73) Broyden, C. G., The Convergence of a Class of Double-rank Minimization Algorithms 1. General Considerations. *IMA J. Appl. Math.* **1970**, 6, 76-90.

(74) Broyden, C. G., The Convergence of a Class of Double-rank Minimization Algorithms 2. The New Algorithm. *IMA J. Appl. Math.* **1970**, 6, 222-231.

(75) Fletcher, R., A New Approach to Variable Metric Algorithms. *Comput. J.* **1970**, 13, 317-322.

(76) Goldfarb, D., A Family of Variable-Metric Methods Derived by Variational Means. *Math. Comput.* **1970**, 24, 23-26.

(77) Shanno, D. F., Conditioning of Quasi-Newton Methods for Function Minimization. *Math. Comput.* **1970**, 24, 647-656.

(78) Enkovaara, J.; Rostgaard, C.; Mortensen, J. J.; Chen, J.; Dułak, M.; Ferrighi, L.; Gavnholt, J.; Glinsvad, C.; Haikola, V.; Hansen, H. A.; Kristoffersen, H. H.; Kuisma, M.; Larsen, A. H.; Lehtovaara, L.; Ljungberg, M.; Lopez-Acevedo, O.; Moses, P. G.; Ojanen, J.; Olsen, T.; Petzold, V. *et al.*, Electronic Structure Calculations with GPAW: A Real-Space Implementation of the Projector Augmented-Wave Method. *J. Phys.: Condens. Matter* **2010**, 22, 253202.

(79) Yan, Y.; Mortensen, J. J.; Jacobsen, K. W.; Thygesen, K. S., Linear Density Response Function in the Projector Augmented Wave Method: Applications to Solids, Surfaces, and Interfaces. *Phys. Rev. B* **2011**, 83, 245122

FIGURES AND TABLES

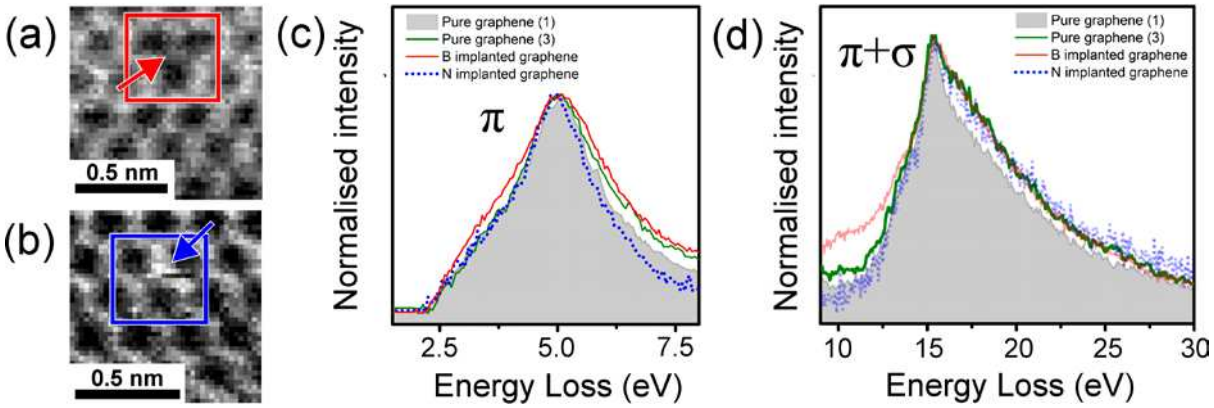

Figure 1. MAADF images of (a) B and (b) N implanted graphene acquired simultaneously with the EEL spectra comprising the integrated spectra in (c, d), showing the position of single substitutional B (a) and N (b) atoms (arrows). Each pixel in (a) and (b) corresponds to an individual spectrum. The hetero-atoms are identified by a characteristic decrease (B) or increase (N) in MAADF image intensity. (c, d) background-subtracted loss spectra of B and N doped graphene compared to those of the non-doped graphene patch shown in Figure 2. The B-implanted patch spectrum was averaged over the region indicated by the red box in (a), while the spectrum of the N-implanted patch was averaged over the region indicated by the blue box in (b). Both regions encompass approximately the same number of atoms. The non-doped graphene spectra were integrated over the regions “1” and “3”, indicated in the MAADF image in Figure 2a.

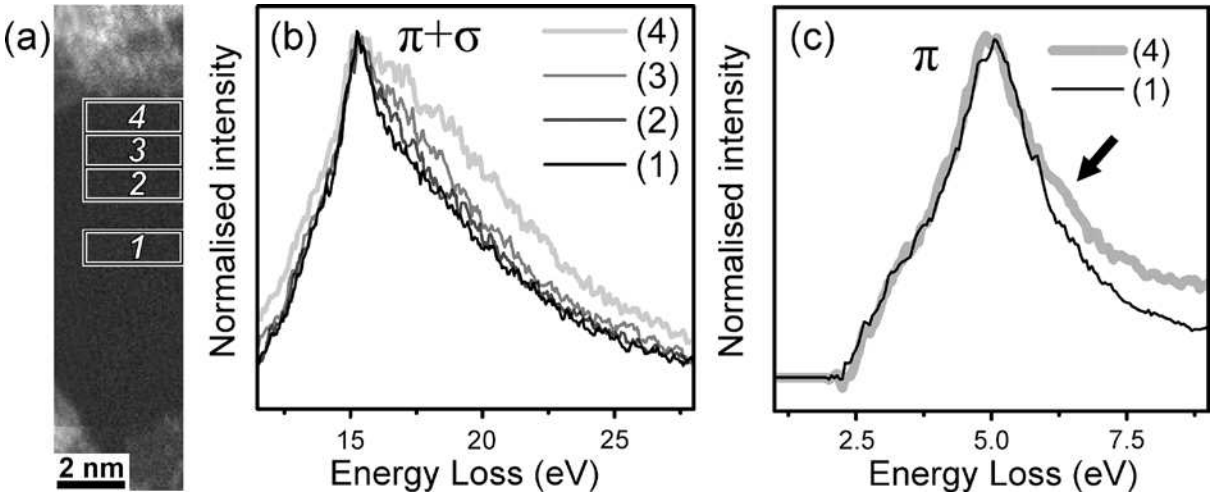

Figure 2. (a) MAADF image of a non-doped single layer graphene patch. (b) background-subtracted loss spectra integrated over regions 1-4 indicated in (a), normalised to the π+σ peak height. (c) Loss spectra integrated over regions 1 and 4 indicated in (a), normalised to the π peak height.

Table 1. Estimated π peak energies and FWHMs, measured using the monochromated Nion UltraSTEM100MC (ΔE = 200 eV). The "non-doped" peak values are measured from spectra integrated over regions "1" and "3" in Figure 2a.

Dopant	π peak FWHM (eV)	π peak E_π (eV)	π-π* "tail" FWHM (eV)	π-π* "tail" E_π (eV)
N	1.50±0.09	5.00±0.01	1.40±0.13	3.47±0.08
None "1"	1.75±0.09	5.07±0.01	1.33±0.07	3.40±.0.07
None "3"	1.80±0.10	5.04±0.01	1.20±0.06	3.40±.0.05
B	2.17±0.09	5.08±0.01	1.23±0.04	3.29±.0.03

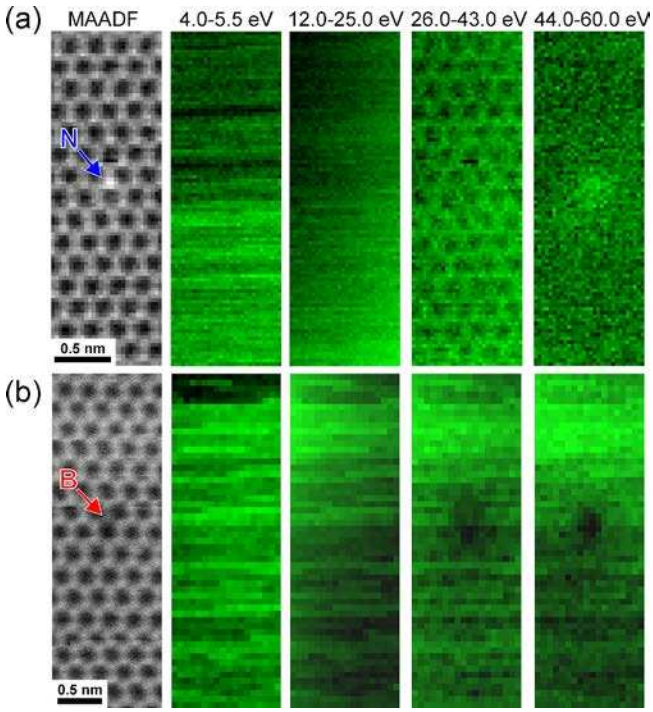

Figure 3. MAADF images and EELS maps integrated from the raw data over the energy regions indicated for (a) N doped (b) B doped graphene.

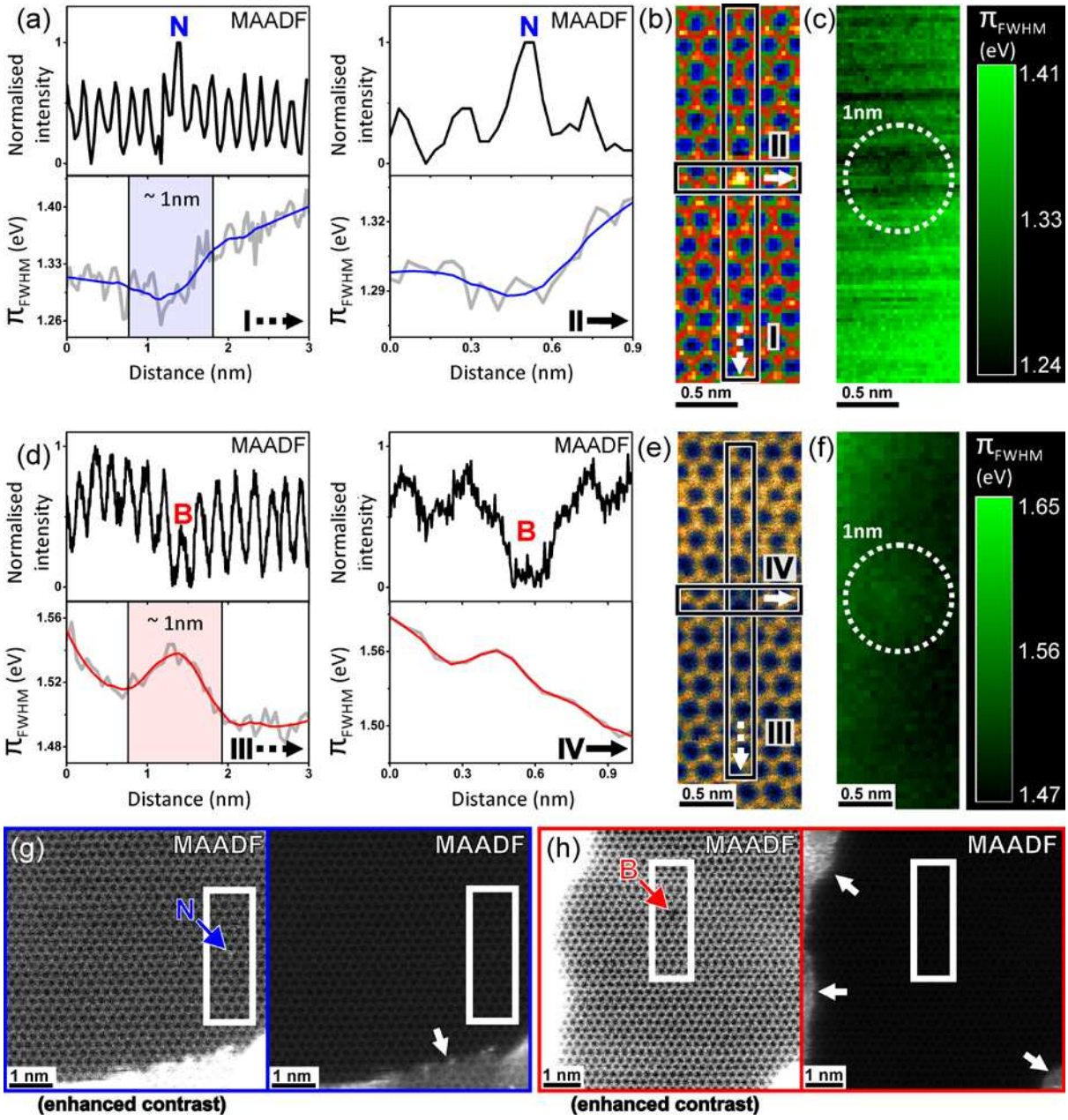

Figure 4. MAADF integrated intensity line profiles compared to the local change in π plasmon peak width (FWHM) for N (a) and B (d) doped graphene. Smoothed FWHM line profiles are superimposed as guides to the eye. The corresponding MAADF images and π plasmon peak FWHM maps are shown in b, c (N) and e, f (B), respectively. The regions from which the line profiles were extracted are indicated. The localisation of the observed π plasmon enhancement (N) and dampening (B) is estimated to be ~1 nm, as indicated in a, c

and d, f, respectively. False colour intensity scales were used for the MAADF images in b, e in order to optimise legibility. Overview MAADF images of the region analysed in a-c and d-f are shown in (g) and (h), respectively. The white rectangles indicate the regions from which the EELS maps were acquired. The contrast is enhanced in the leftmost panels of g and h to optimise the legibility of the individual dopant atoms.

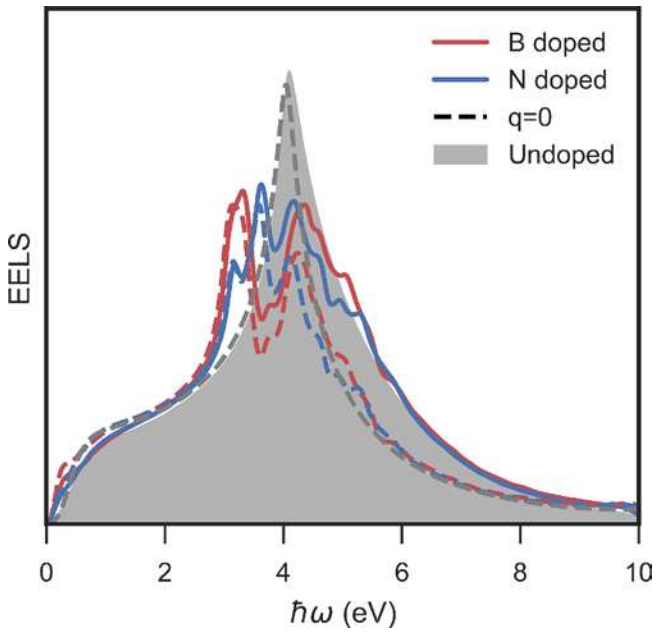

Figure 5. Simulated low-loss EEL spectra comparing B-doped (red), N-doped (blue) and pure graphene (grey). The doped response was calculated in 3x3 supercells with a single dopant atom. The electronic doping has been adjusted to the Dirac point (for the B/N-doped systems) to reflect the low doping level in the experimental system. Full lines show the full $\vec{q}$-summed EEL spectrum while the dashed lines show the q = $|\vec{q}| = 0$ response, *i.e.* in the optical limit without local field effects. The shaded region shows the simulated EEL spectrum for un-doped graphene.

TABLE OF CONTENTS GRAPHIC

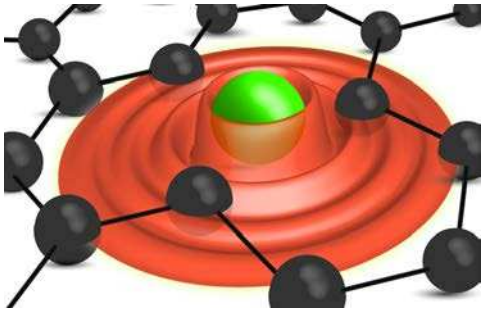

COVER GRAPHIC SUGGESTION

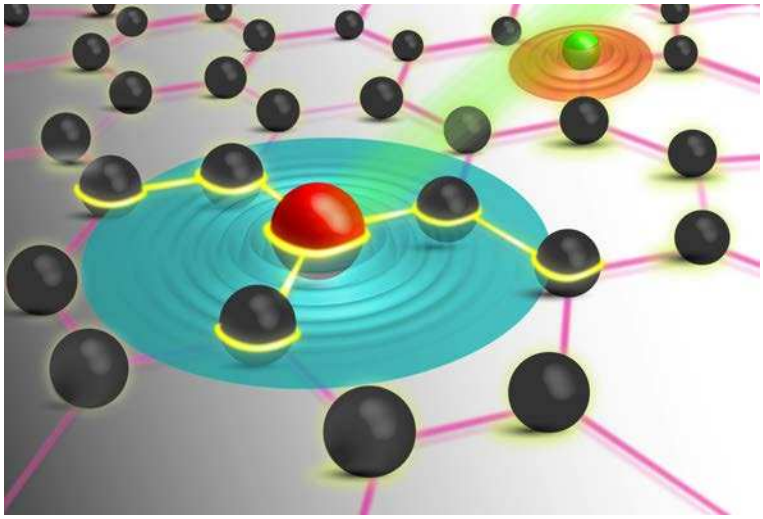

Supporting Information:
Local Plasmon Engineering in Doped Graphene

Fredrik S. Hage,[*,†] Trevor P. Hardcastle,[†,‡] Morten N. Gjerding,[§] Demie M. Kepaptsoglou,[†,△] Che R. Seabourne,[‡] Kirsten T. Winther,[§] Recep Zan,[⊥] Julian Alexander Amani,[¶] Hans C. Hofsaess,[¶] Ursel Bangert[‖], Kristian S. Thygesen[§] and Quentin M. Ramasse[*,†,‡,▲]

[†]SuperSTEM Laboratory, SciTech Daresbury Campus, Daresbury, WA4 4AD, U.K.
[‡]School of Chemical and Process Engineering, University of Leeds, Leeds, LS2 9JT, U.K.
[§]CAMD and Center for Nanostructured Graphene (CNG), Denmark Technical University, Fysikvej 1, building 307, 2800 Kgs. Lyngby, Denmark.
[△]York NanoCentre, University of York, Heslington, York, YO10 5BR, U.K.
[⊥]Nanotechnology Application and Research Center, Niğde Omer Halisdemir University, Niğde 51000, Turkey.
[¶]II Physikalisches Institut, Georg-August-Universität Göttingen, Friedrich-Hund-Platz 1, 37077 Göttingen, Germany.
[‖]Bernal Institute and Department of Physics, University of Limerick, Limerick, Ireland.
[▲]School of Physics, University of Leeds, Leeds, LS2 9JT, U.K.

[*]Corresponding addresses: qmramasse@superstem.org, fshage@superstem.org

CORE LOSS EELS MAPS OF DOPANTS (NUS100MC)

In following with Bangert *et al.*[1] the B and N dopants shown in Figure 1a, b were mapped using the EELS B-*K* and N-*K* ionisation edges. The resulting maps are shown in Figure S1 and independently verify the presence of substitutional B and N atoms in the graphene lattice.

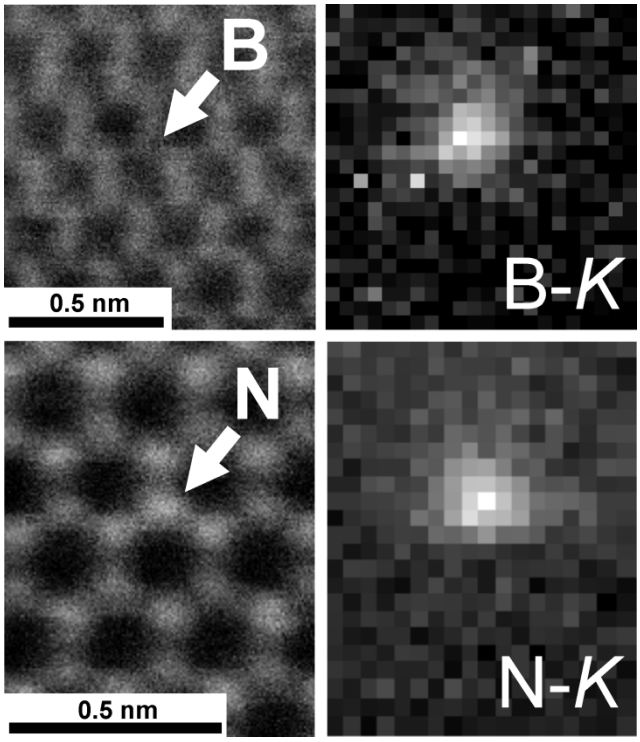

Figure S1. MAADF images (left) and core loss EELS maps (right) identifying a single substitutional B or N heteroatom dopant in single layer sheets of graphene. The data were acquired using the NUS100MC microscope.

ENERGY RESOLUTION AND INSTRUMENTAL BROADENING (NUS100MC)

The NUS100MC microscope allows for varying the energy resolution from 400 meV to 13 meV, while maintaining atomic image resolution.[2, 3] Figure S2 shows the effect of increasing energy resolution from 400 meV to 80 meV on spectra acquired from a non-doped graphene patch. Spectra normalised to the ZLP height are shown in Figure S2a, while

spectra normalised to the π peak are shown in Figure S2b. Upon increasing the energy resolution from 400 meV to 200 meV, there is a significant reduction in π peak width and ZLP tail contribution. Increasing the resolution from 200 meV to 80 meV results in a minor reduction in the ZLP tail contribution but in no significant decrease in π peak width. Thus it is suggested that for ΔE ≤ 200 meV, the π peak width reflects primarily the associated excitation lifetime,[4] meaning the effect of instrumental broadening is deemed negligible. As increasing the energy resolution results in an accompanying reduction of available beam current (*i.e.* if keeping other microscope parameters unchanged),[5] the NUS100MC spectra in Figures 1, 2 were acquired at ΔE = 200 meV in order to optimise the signal-to-noise ratio.

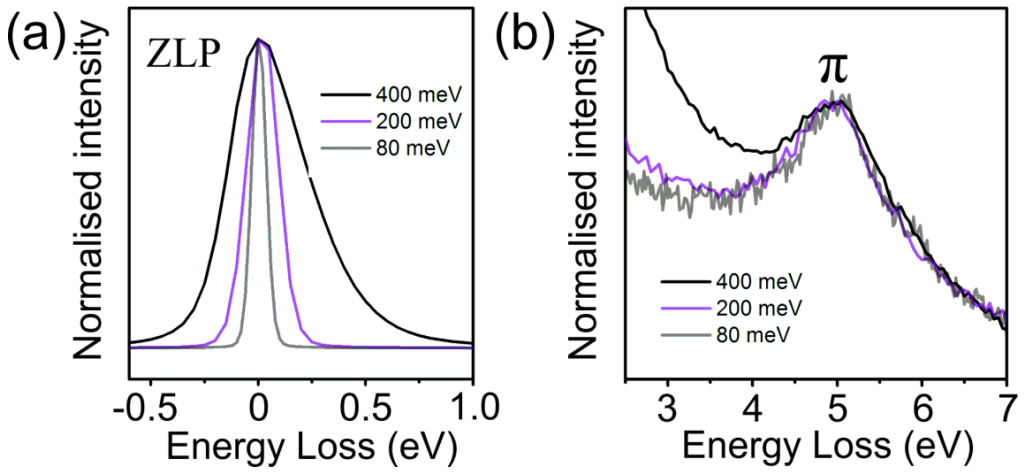

Figure S2. (a) Zero loss peaks and (b) loss spectra normalised to the π peak height of a non-doped single layer graphene patch at three different energy resolutions (400 meV, 200 meV and 80 meV). No decrease in π peak width can be observed in (b) when increasing the energy resolution from 200 meV to 80 meV. The data were acquired using the NUS100MC microscope.

VALENCE LOSS SPECTRA (NUS100)

Figure S3c shows background subtracted normalised valence loss spectra, acquired using the NUS100 microscope, while Figure S3a (b) shows HAADF images and accompanying intensity line profiles confirming the presence of an individual B (N) dopant.[1] As discussed above, instrumental broadening is deemed negligible for the π peak width measurements using the NUS100MC (ΔE = 200 meV), so the measured differences in π peak width in Table 1 correspond directly to dopant-induced changes in excitation lifetime. For the NUS100 microscope measurements, instrumental broadening contributes to absolute π peak widths due to a comparatively poorer energy resolution (ΔE = 350 meV). However, π peak width changes induced by doping measured with the NUS100 microscope (see Table S1) are clearly in good qualitative agreement with those measured with the NUS100MC (see Table 1). As we observe the same trend in dopant induced π peak modification in Figure 1c and Figure S3 on two different microscope systems (at different energy resolutions and spectrometer collection angles, see Methods) instrumental factors are highly unlikely to be the origin of this effect.

Note that while the dopant-free NUS100MC spectra (Figures 1c, d, and 2 c, d) were acquired from a non-doped reference sample (see Methods), the corresponding NUS100 spectrum (Figure S3c) was acquired from a patch of the otherwise B-doped sample that was deemed devoid of dopants upon inspection of the relative HAADF image intensities of each carbon atom of the patch (shown in Figure S4). The good qualitative agreement between non-doped NUS100MC (Figure 1c) and NUS100 (Figure S3c) π peak loss spectra, with respect to the effect of doping, indicates that any possible contribution from any B dopants present beyond the confines of the dopant free single layer patch in Figure S4 is negligible for the

non-doped spectrum in Figure S3c. This agrees well with the ~1 nm localisation estimate in Figure 4.

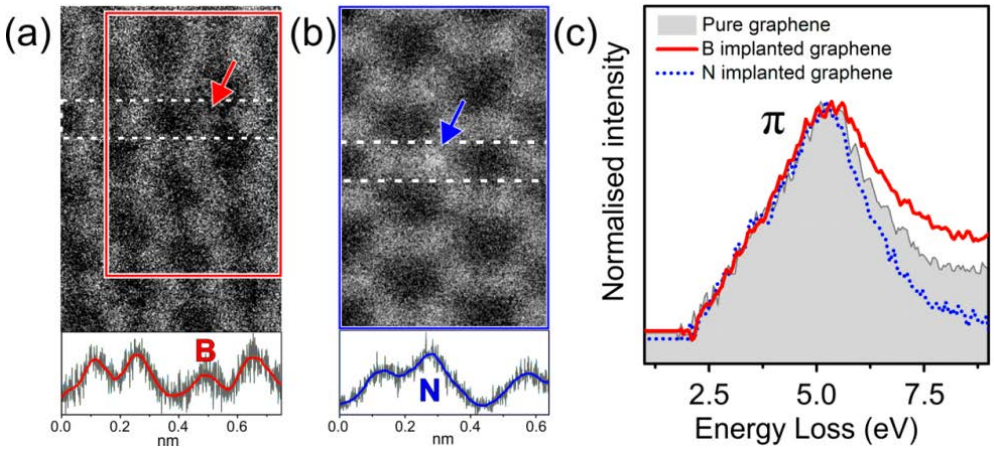

Figure S3. HAADF images of (a) B and (c) N implanted graphene acquired simultaneously with the EEL spectra in (c), showing the position of single substitutional B (a) and N (b) atoms (arrows). The hetero-atoms are identified by a characteristic dip (B) or increase (N) in the HAADF intensity profiles integrated over the area indicated by the dashed rectangles superimposed on the images. (c) background-subtracted loss spectra of B and N doped graphene compared to that of a non-doped graphene patch. The B-implanted spectrum was averaged over the region indicated by the rectangular box in (a), while the N-implanted spectrum was averaged over the entire region shown in (b), both regions encompass approximately the same number of atoms. All data were acquired using the NUS100 microscope.

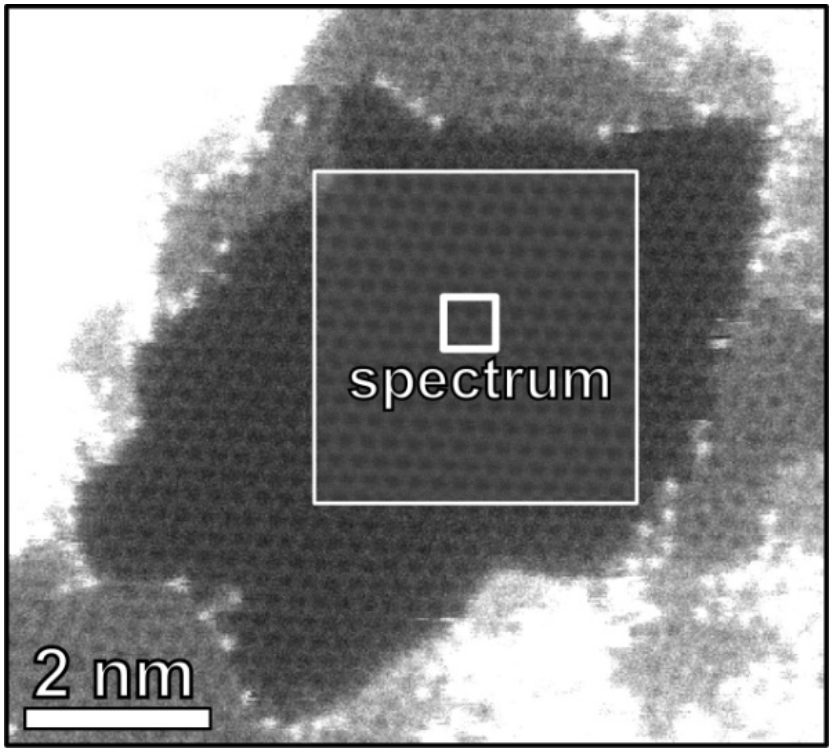

Figure S4. HAADF image of the patch from which the dopant-free graphene spectrum in Figure S3c was acquired. The larger white square shows the superimposed HAADF image acquired simultaneously with the full valence EEL spectrum image. The smaller white square indicates the region over which the dopant-free graphene spectrum in Figure S3c was integrated. Data were acquired using the NUS100 microscope.

Table S1 Estimated π peak energies and FWHMs, measured using the NUS100 (ΔE = 350 meV).

Dopant	π peak FWHM (eV)	π peak E_π (eV)	π-π* "tail" FWHM (eV)	π-π* "tail" E_π (eV)
N	1.96±0.03	5.22±0.01	1.54±0.03	3.44±0.03
None	2.21±0.04	5.30±0.03	1.54±0.02	3.38±.0.05
B	2.92±0.06	5.33±0.02	1.12±0.1	3.24±.0.03

ADDITIONAL AB INITIO EELS CALCULATIONS

Extensive preliminary calculations of the valence response of B- and N-doped graphene were carried out with a number of supercells. As with the calculations in the main text, these were carried out within density functional theory (DFT) and invoke invoke corrections for Local Field Effects (LFEs) to the Random Phase Approximation (RPA) loss function, on supercells of sizes 2x2 and 3x3, with hexagonal and honeycomb superlattices of B and N dopants up to +15 eV above the Fermi energy. Calculations on 4x4 supercells were attempted but failed due to excessive memory requirements. Monkhorst-Pack *k* point grids of 18x18x1 and 12x12x1 were used for the 2x2 and 3x3 reciprocal cells, chosen systematically to allow for the exact same $\vec{q}$ vectors to be compared across the cells of different size. Unlike the final spectra presented in the main manuscript, these did not include a correction for the modified carrier concentration induced in the ground state by the presence of the dopant. This more simple approach led to the appearance at low energy (approximately 1 eV) of a sharp peak in the doped graphene spectra, which is most intense at q = 0. As discussed in the main text, the sharp nature of these features, and the fact that they are not affected by the inclusion of higher momentum transfers in the calculation, suggest these can likely be attributed to single $\pi \rightarrow \pi^*$ transitions involving states created as an artefact due to the finite supercell size for the doped systems.

This series of initial calculations is reproduced below in Figure S5 for completeness and to provide a benchmark for further improvement of DFT-based calculations of doped graphene systems.

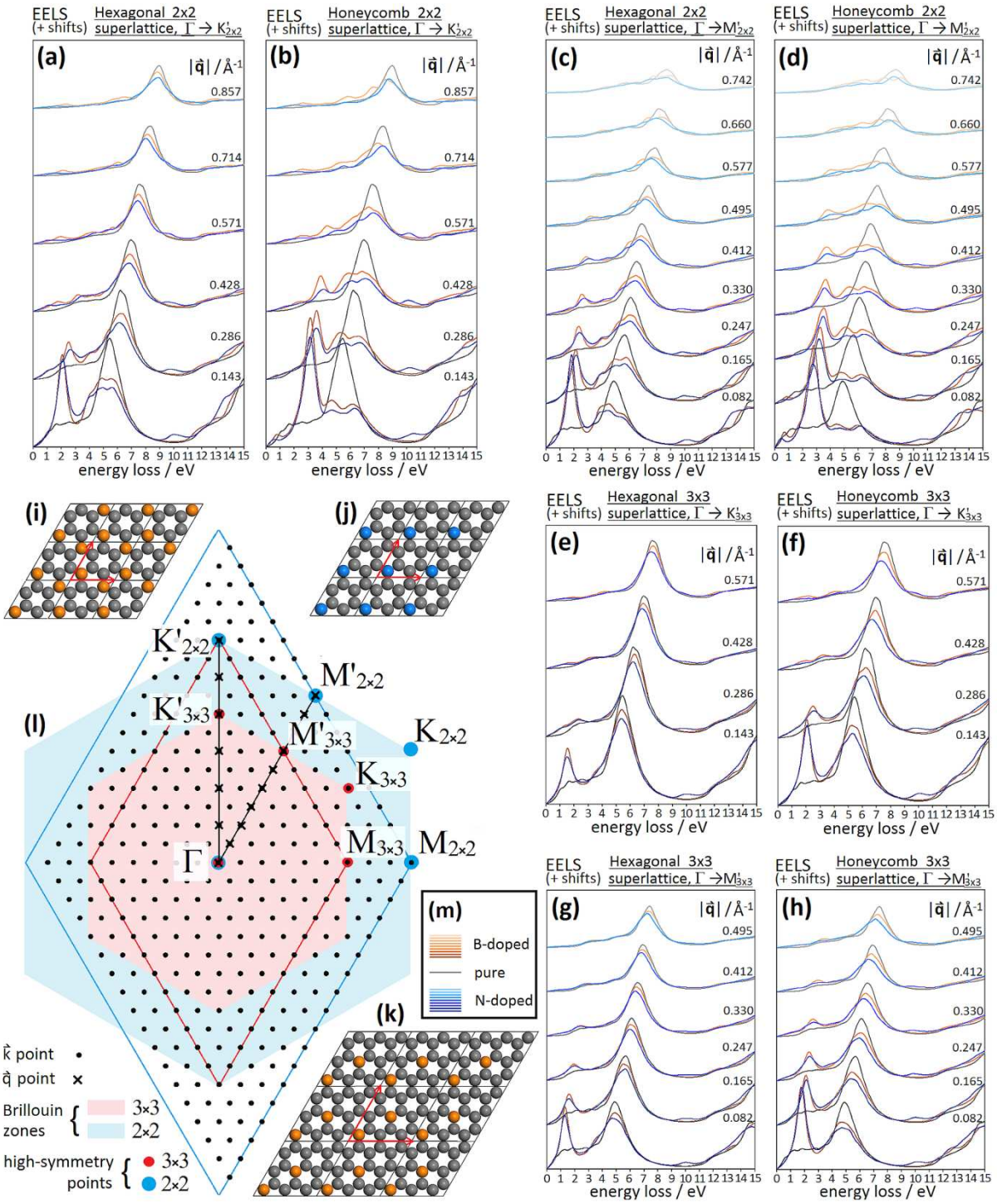

Figure S5. Series of calculations (a-h) of the valence response of pure graphene (grey lines), N-doped graphene (blue lines) and B-doped graphene (orange lines), carried out at different momentum transfer q as indicated on the individual panels. The various supercell geometries used for the calculations are also summarised in the models (i-k).

REFERENCES

(1) Bangert, U.; Pierce, W.; Kepaptsoglou, D. M.; Ramasse, Q.; Zan, R.; Gass, M. H.; Van den Berg, J. A.; Boothroyd, C. B.; Amani, J.; Hofsäss, H., Ion Implantation of Graphene—Toward IC Compatible Technologies. *Nano Lett.* **2013**, 13, 4902-4907.

(2) Ramasse, Q. M., Twenty Years After: How “Aberration Correction in the STEM” Truly Placed a “A Synchrotron in a Microscope". *Ultramicroscopy* **2017**, 180, 41-51.

(3) Nicholls, R.; Hage, F. S.; Yates, J.; McCulloch, D.; Kepaptsoglou, D. M.; Lovejoy, T. C.; Dellby, N.; Krivanek, O. L.; Refson, K.; Ramasse, Q. M., Vibrational Phonon Spectroscopy of Boron Nitride Polymorphs: A Comparison Between Theory and Experiment. *Microsc. Microanal.* **2015**, 21, 1469-1470.

(4) Egerton, R. F., *Electron Energy-Loss Spectroscopy in the Electron Microscope*. Springer US: New York, 2011.

(5) Krivanek, O. L.; Ursin, J. P.; Bacon, N. J.; Corbin, G. J.; Dellby, N.; Hrncirik, P.; Murfitt, M. F.; Own, C. S.; Szilagyi, Z. S., High-Energy-Resolution Monochromator for Aberration-Corrected Scanning Transmission Electron Microscopy/Electron Energy-Loss Spectroscopy. *Philos. Trans. Royal Soc. A: Math. Phys. Eng. Sci.* **2009**, 367, 3683-3697.